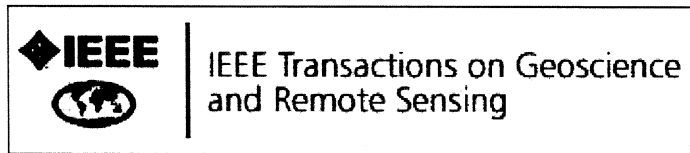


Sun Glint and Sea Surface Salinity Remote Sensing

Emmanuel P. Dinnat and David M. Le Vine
Instrumentation Sciences Branch
Goddard Space Flight Center
Greenbelt, MD 20771

Popular Summary

A new mission in space, called Aquarius/SAC-D, is being built to measure the salinity of the world's oceans. Salinity is an important parameter for understanding movement of the ocean water. This circulation results in the transportation of heat and is important for understanding climate and climate change. Measuring salinity from space requires precise instruments and a careful accounting for potential sources of error. One of these sources of error is radiation from the sun that is reflected from the ocean surface to the sensor in space. This paper examines this reflected radiation and presents an advanced model for describing this effect that includes the effects of ocean waves on the reflection.



Sun Glint and Sea Surface Salinity Remote Sensing

Journal:	<i>Transactions on Geoscience and Remote Sensing</i>
Manuscript ID:	draft
Manuscript Type:	IGARSS 2007 Special Issue paper
Date Submitted by the Author:	n/a
Complete List of Authors:	Dinnat, Emmanuel; NASA/GSFC, Laboratory for Hydrospheric Processes Le Vine, David; NASA, GSFC
Keywords:	Microwave radiometry, Remote sensing



Sun Glint and Sea Surface Salinity Remote Sensing

Emmanuel P. Dinnat

Goddard Earth Science and Technology Center
University of Maryland Baltimore County
NASA Goddard Space Flight Center
Greenbelt, MD 20771

David M. Le Vine

Instrumentation Sciences Branch
Goddard Space Flight Center
Greenbelt, MD 20771

Abstract—The Aquarius/SAC-D mission will employ three L-band (1.41 GHz) radiometers dedicated to remote sensing of Sea Surface Salinity. The mission will be in a dawn/dusk sun-synchronous orbit with the beam oriented toward the night side of the orbit in order to limit interference from the Sun. In this manuscript, the influence of Sun radiation reflected at the Earth surface is examined for its dependence on the surface roughness. It is shown that the reflected Sun radiation can be separated into two components: (a) A quasi-specular component which has a large brightness temperature but is located far from the antenna boresight; and (b) A scattered component, due largely to small-scale roughness, which has relatively small brightness temperature, but can extend into the antenna boresight, where the gain is maximum, during some portion of the orbit at some times of the year. The latter component induces the largest (and the only critical) contamination of the measurements. It is shown that that significant contamination is possible at high latitude close to the summer solstice, when the antenna footprint is not in shadow.

Keywords—component; sea surface salinity, sun glint, L-band, Aquarius

I. INTRODUCTION

The Aquarius/SAC-D mission is dedicated to the remote sensing of Sea Surface Salinity (SSS) and is to be launched in 2009 [1]. An L-band (1.41 GHz) radiometer, with three beams pointing at 25.8°, 33.8° and 40.3° off the nadir (see Figure 1.), is the core instrument for retrieving SSS. The accuracy required on the radiometric measurements for retrieving SSS within the required 0.2 practical salinity unit (psu) is about 0.1 Kelvin (K). An important potential source of noise that could hinder this accuracy is the Sun. The Sun brightness temperature at L-band is three orders of magnitude larger than that of the ocean. It ranges mostly from 100,000 K to 500,000 K depending on the solar activity (see section II.C), whereas the ocean brightness temperature is in the range 70-110 K at the incidence angles of Aquarius. The approach followed to minimize the Sun contamination was to adopt a dusk/dawn (6 PM/AM ascending/descending equatorial crossing) sun-synchronous orbit, and to orient the antenna beams towards the night side of the Earth surface. Doing so, the Sun is in the direction of the antenna back lobes and the specular reflection of the Sun radiation does not come through the main beam. In addition, the Aquarius antennas have been specifically

designed to offer a gain as low as possible in the direction of the direct and specularly reflected radiation. However, the ocean surface is rough and during certain seasons the footprint is not in shadow. Hence, the reflection is not truly specular and the possibility that scattered solar radiation can induce a significant signal requires investigation.

First, even in the ideal case where the Sun is oriented at a right angle with the Aquarius orbit plane, and therefore the antennas always point towards the night side, a significant part of earth visible to the antenna is on the day side. That means that Sun radiation scattered towards the antenna side-lobes can come from relatively large area if one accounts for the roughness of the ocean surface.

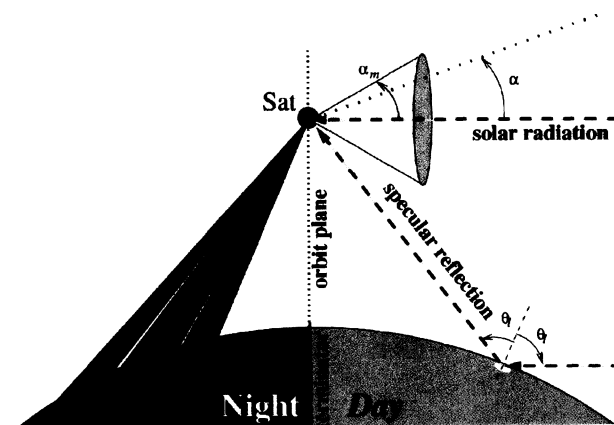


Figure 1. 2D sketch of the measurements geometry. The satellite is at the location marked Sat. The main beams of the three antenna (red in the figure.) point towards the night side of the Earth. The Sun direct radiations (upper dashed line arrow) come at right angle with the satellite orbit plane (the vertical dashed line) in this case, but can come at any elevation angle α in the cone of aperture $\alpha_m = 32^\circ$. The Sun radiations specularly reflected on the Earth surface are illustrated by the lower dashed-line arrow.

Second, the satellite orbit is rarely aligned exactly on the terminator, and in actuality, the Sun direction varies significantly (illustrated by the cone of aperture α in Figure 1.). When the Sun elevation increases, the illuminated area shifts towards the antenna boresight (i.e. the left side in the figure), and the antenna can actually point to the day side during some portions of the orbits. In this case, because the surface is rough, some Sun radiation can be scattered back into the main beam where the gain is the largest.

Yueh et al. made a preliminary study of the potential Sun glint contamination on an Aquarius-like radiometer [2]. Using simplifying hypothesis regarding the antenna gain and the scattering at the surface, they derived an order of magnitude for the maximum contamination of 0.1 K to 10 K, depending on the solar activity. However, these values were derived for a worst case scenario, where the antenna is pointing towards the day-side. It certainly shows that the Sun is a potential issue for L-band radiometry, and that pointing towards the Sun should be avoided. Unfortunately, it does not provide an estimate for the contamination in the realistic case of a night-side pointing mission like Aquarius/SAC-D. Le Vine et al. [3] account for the proper geometry for the mission and find a total contamination (i.e. direct and reflected rays from the Sun) up to 0.1 K. However, they assume specular reflection (smooth surface) and do not account for the presence of land surfaces in the antenna field of view (FOV). They also report the combined influence the direct and reflected ray which makes it hard to identify the sole contribution of the later. Finally, Reul et al. estimate the effect of the Sun on the Soil Moisture and Ocean Salinity (SMOS) mission [4], which is also an L-band radiometer, but with a very different geometry (orbit and antenna pointing direction) and technology. The SMOS instrument is a two dimensional interferometer used to produce images of the surface T_b of large spatial coverage (of the order of 1000 km), half of the image being over the day-side. The range of incidence angles of the measurements is also very different than those of Aquarius. They find contaminations up to 50 K during the winter solstice at high latitudes of the southern hemisphere.

The objective of this study is to determine if Sun glint is an issue for remote sensing of SSS with a conventional radiometer and geometry such as will be flown on Aquarius. First the impact of various scales of surface roughness on the Sun radiation scattered toward the satellite is discussed to illustrate the circumstances under which the contamination can be significant. Then we derive estimates for the Sun glint contamination, and emphasize when in a year and where on the globe the glint is large enough to potentially hinder retrieval of SSS. In section II, we describe the geometry of the problem and the models we have employed for computing the reflected Sun radiation and the resulting antenna temperature. In Section III, we present the results of the numerical computations. We first report the results for synthetic cases, as a function of the Sun position with respect to the satellite only. Then the results are reported in terms of geographical location and time of the year.

II. MODELLING INFLUENCE OF THE REFLECTED SUN ON THE MEASUREMENTS

A. Geometry of the Sun contamination

We use simulations of the Aquarius/SAC-D orbit (JPL, personal communication) to locate the satellite in the Earth Centered Inertial (ECI) coordinate system (epoch J2000) during the year 2009 at a time resolution of up to 1 seconds. We also calculate the Sun position in the ECI at the same times. Figure 2. shows the angle between the Sun direction

and 1) the antenna boresight for the inner beam (the one pointing the closest to the Sun) and 2) the angular momentum vector of the satellite (α angle in Figure 1.).

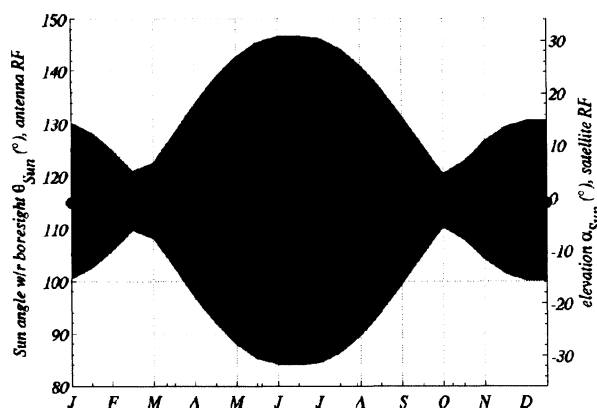


Figure 2. left y-axis: angle between the antenna boresight of the inner beam and the Sun direction for one year (2009, the month initial is reported on the x-axis). The dots report a two-week average, the bars the RMS of the variation during these 2 weeks and the greyed area the total range of variation of the angle. Right y-axis: Sun elevation angle with respect to the orbit momentum axis (α in Figure 1.). Note that the elevations are approximates, as for a given angle on the left x-axis, there exist various α differing by a few degrees depending on the azimuth angle.

On average $\alpha \sim 90^\circ$, meaning that the Sun is at right angle with the orbital plane. At this location, the antenna main beams are not in the illuminated area. However, the results show that large displacements around the average value can occur, especially at the winter solstice ($\pm 15^\circ$ around the mean) and even more at the summer solstice ($\pm 30^\circ$). During the positive sign extrema, when the satellite is at the high latitudes of the Northern hemisphere, the illuminated portion of the FOV extends beyond the antenna boresights. At the equinoxes, the direct ray is almost normal to the plane of the orbit ($\pm 3^\circ$) and the Sun is at an optimal position. In all cases, the direct ray from the Sun is very far from the boresight (more than 85° off it) and it appears in the far sidelobes of the antenna pattern. The issue of the contamination by the direct Sun has already been discussed [3] and remains an antenna design issue that will not be addressed in this paper.

In the calculations reported here, the intersection of the antennas FOV's with the Earth surface (referred hereafter as the visible disk) is computed. The visible disk has a diameter of the order of 5000 km on the Earth surface. The illuminated area on the Earth surface is also computed from the position of the Sun, and the intersection between the visible disk and the illuminated area (referred hereafter as the illuminated FOV) is retained for the computations. The local incidence and azimuth angles for rays from the Sun and to the satellite are then computed for each point over the entire illuminated FOV. This is done at the angular resolution of the antenna pattern (see section II.D). This provides the bistatic configuration for the incident and scattered radiations needed for computing the scattering intensities.

B. Surface reflectivity and antenna temperatures

In all the following, we assume homogeneous sea surface temperature (15°C) and salinity (35 psu). The influence of these parameters on the results is expected to be small because of their relative small influence on the reflection and scattering coefficients. We compute the antenna temperature induced by the Sun radiations after reflection from the Earth surface (referred hereafter as the Sun glint T_a) using three different hypotheses: (1) Assuming specular reflection (a smooth surface); (2) Using geometrical optics to compute the scattered radiation from a rough surface; and (3) Using a two-scale model to include the effect of small scale roughness. These various approaches allow us to understand how the various roughness scales influence the final results and their relative importance.

1) The specular model

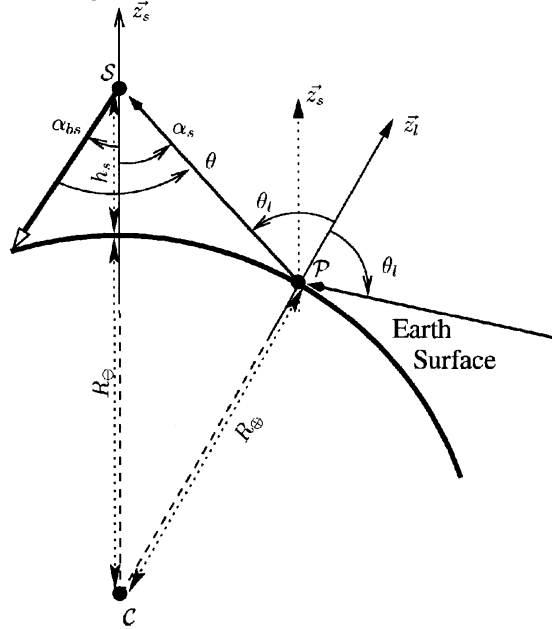


Figure 3. geometry for the scattering at the surface. The satellite is at the location S at an altitude h_s above the Earth surface, the antenna beam points toward the left side at an angle α_{bs} with respect to the nadir direction. Radiation is coming to the antenna from the location P on the surface, after specular reflection (i.e. the local incidence angle θ_l is the same for the incoming and emerging radiation).

Specular reflection is assumed, obeying Fresnel's laws in a plane tangent to the surface at the point of reflection. The Earth curvature is taken into account. There is at most one point on the Earth surface, the specular point, where the satellite and the Sun share the same plane of incidence and the same incidence angle with respect to the local normal. In this case, the Sun glint antenna temperature (T_a) is computed as [3]:

$$T_a = G(\theta, \phi) R(\theta_l) T_b \Omega_{\square} / 4\pi \quad (1)$$

where θ and ϕ are the spherical coordinates of the specular point in the antenna reference frame, G is the antenna gain in that direction and R is the surface Fresnel reflection coefficient, at the local incidence angle θ_l . Ω_{\square} and T_b are the Sun solid angle (assumed to be conserved after reflection) and brightness temperature, respectively, and are discussed in section C. The local incidence angle at the surface of a radiation coming from the direction (θ, ϕ) is given by (see Figure 3.)

$$\theta_l = \sin^{-1}(-\sin \alpha_s (R_{\oplus} + h_s) / R_{\oplus}) \quad (2)$$

with h_s the altitude of the satellite, R_{\oplus} the radius of the Earth and the angle α_s between the incoming radiation and the nadir direction given by

$$\alpha_s = \pi - \cos^{-1}(\sin \theta \sin \phi \sin \alpha_{bs} + \cos \theta \cos \alpha_{bs}). \quad (3)$$

The angle α_{bs} is the boresight elevation.

2) The geometric optics model

In this approach, a geometrical optics (GO) model is used to account for the tilting of the local surface due to the large-scale ocean waves. The model is valid only for waves with wavelength larger than $\sim 4\lambda$ (i.e. 84 cm) and, therefore, a significant portion of the roughness scale is ignored. Contrary to the smooth surface, in this case any point on the illuminated surface can potentially reflect the Sun specularly towards the satellite if the tilt of the local surface due to the waves is in the proper direction. We first compute the tilting angles required to put the satellite and the Sun in a specular configuration for each location in the illuminated FOV. The tilting angles are then converted into so-called wave 'specular' slopes in the upwind (S_u) and crosswind (S_c) direction. The contribution of each location to the T_a will then be weighted by the probability of occurrence of the wave with the specular slopes. To derive this probability, we assume that the probability density function (PDF) of the waves with slopes S_u and S_c is a zero-mean Gaussian function and is given by

$$P(S_u, S_c) = \frac{1}{2\pi\sigma_{Su}\sigma_{Sc}} \exp \left\{ -0.5 \left[\left(\frac{S_u}{\sigma_{Su}} \right)^2 + \left(\frac{S_c}{\sigma_{Sc}} \right)^2 \right] \right\} \quad (4)$$

where σ_{Su} and σ_{Sc} are the RMS of the slopes of waves with a wavelength larger than 4λ . The T_a is then derived by integration of the weighted local reflectivity over the entire illuminated area:

$$T_a = \iint_{FOV} G(\theta, \phi) R^*(\theta_l, \phi_l) T_b \frac{\Omega_{\square}}{4\pi} \sin \theta d\theta d\phi \quad (5)$$

with the weighted local reflectivity

$$R^*(\theta_l, \phi_l) = R(\theta_l') \Omega_w(S_x, \theta_l) P(S_u, S_c) J(\theta, \phi) \quad (6)$$

where θ_l^i is the local incidence of the satellite and the Sun with respect to the normal of the tilted surface, $J(\theta, \phi)$ is the Jacobean determinant that converts the differential term $\sin \theta d\theta d\phi$ into $dS_u dS_c$ and $\Omega_w(S_x, \theta_l^i) = 1 - S_x / \tan(\theta_l^i)$ is the solid angle from the satellite for the wave of slope S_x in the satellite direction.

According to (4), the *PDF* is the largest at the specular point, where the slopes for the specular waves are zero. Therefore the weighting of the local reflection is also the largest at the specular point. The further from the specular point is a location in the illuminated FOV, the lower is the value of *PDF* at that point, and so is the weight for the reflected radiation. Basically, the glint that was concentrated in the close vicinity of the specular point direction when the surface was assumed to be smooth is now spread over a broader area with size determined by the slopes RMS but with an exponential decrease in intensity from the center to the edge of the Sun image. However, that does not mean that the local contribution to T_a given by the integrand in (5) necessarily decreases the same way as the *PDF* does, because the changes in θ_l^i and the antenna gain will also modulate the contribution of the individual integration points.

3) The Two-scale model

To account for all the scales of ocean waves we use a two scale model (*TSM*). In this approach [5] the scattering induced by the small scales is computed using the small perturbation method (*SPM*), and this is modulated by the tilting induced by the large-scales. The two-scale reflection coefficient I_{2s} to be applied to the Sun T_b before integrating over the illuminated FOV is then:

$$T_a = \iint_{FOV} G(\theta, \phi) I_{2s} T_b \sin \theta d\theta d\phi \quad (7)$$

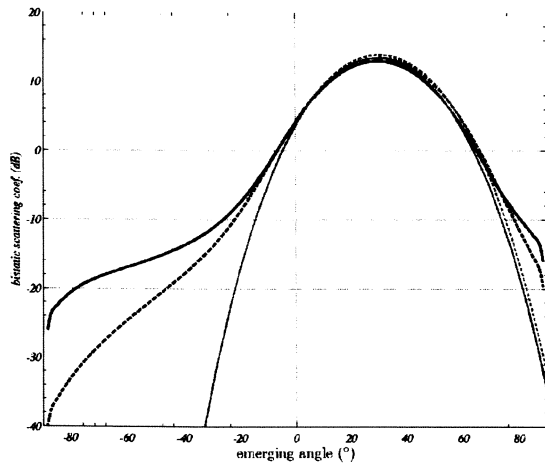


Figure 4. scattering coefficients for an incidence angle of -30° versus the emerging angle. The models are two scale model (black lines) and geometric optic (grey lines), in v-pol (plain line) and h-pol (dashed line). Azimuth angles are the same for the incident and scattered radiations. Note that the specular

model could be represented as a dirac function at scattering angle $+30^\circ$. The wind speed is 8 m/s at 10 m height.

where the two-scale reflectivity is given by

$$I_{2s} = \iint \frac{\sigma^0(\theta_l^i, \phi_l^i; \theta_l^s, \phi_l^s)}{\cos \theta_l^i} \Omega_w P(S_u, S_c) \frac{\Omega_{\square}}{4\pi} dS_u dS_c \quad (8)$$

and results from the integral over the slopes *PDF* of the *SPM* scattering coefficients σ^0 for local incident (θ_l^i, ϕ_l^i) and scattered (θ_l^s, ϕ_l^s) directions [6] (here σ^0 is the sum of copol and crosspol term).

An example of scattering coefficients for the *GO* and *TSM* (i.e. R^* and I_{2s} both normalized by $4\pi \cos \theta_l^s / \Omega_{\square}$) is reported in Figure 4. for a radiation incident at an angle -30° . Both models are relatively close around the specular reflection direction (i.e. radiation emerging at $+30^\circ$). Away from the specular direction, the *GO* model falls off rapidly whereas the *TSM* predicts significant scattering at large emerging angles, particularly in v-pol, because of the influence of the small-scale roughness. Scattering in h-pol falls much faster than in v-pol and is less than in v-pol, particularly at angles far from the specular direction.

C. The Sun Emission

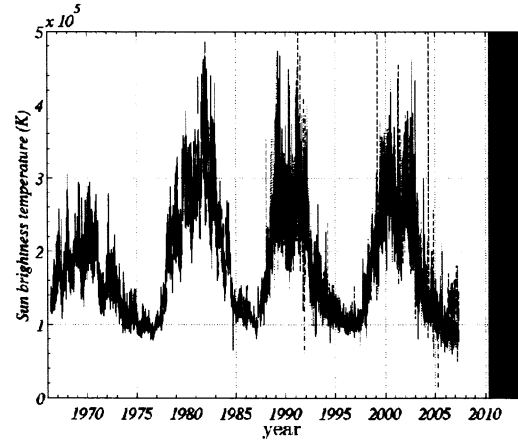


Figure 5. Sun effective brightness temperature derived from the flux measurements by the U.S. Air Force at noon time. Measurements were performed at various sites (reported by different linestyles). The projected Aquarius/SAC-D operation time (May 2010-2013) is reported by the greyed area.

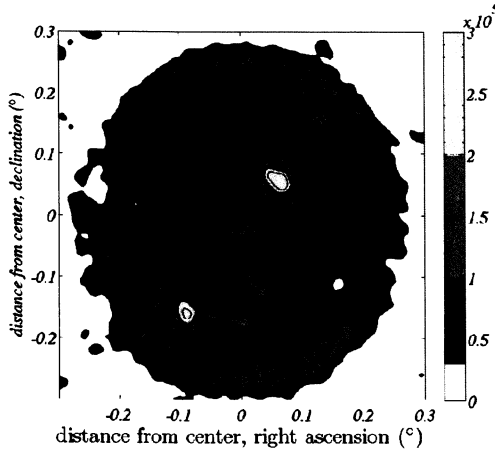


Figure 6. Sun brightness temperature map (K) at 20 cm wavelength measured from the Very Large Array (S. White, personal communication) during a period of low solar activity (July 6th, 1996).

Emission from the Sun at L-band is complex, but reasonably well modeled as a thermal source [3][4]. Figure 5 shows the effective brightness temperature and its variation with the solar cycle derived from the solar flux measured at the U.S. Air Force Radio Solar Telescope Network (RSTN)[7][8]. Although the brightness temperature is not constant over the solar disc (Figure 6.), the solid angle subtended by the sun

$$\Omega_{\square} = 2\pi [1 - \cos \alpha_{\square}] \quad (9)$$

where $\alpha_{\square} = 0.3^{\circ}$ at L-band is small compared to the resolution of the Aquarius antenna. The Sun will be considered as an homogeneous source of solid angle Ω_{\square} .

The Sun effective T_b exhibits large variations (Figure 5.) but is mostly between 100,000K and 500,000K. The variations follow a cycle of approximately 11 years and it is projected that Aquarius will operate near a period of maximum solar activity. Since we want to determine if the Sun glint is a potential issue, we choose $T_b = 5 \times 10^5$ K in order to provide a reasonable upper bound for the contamination.

D. The antenna gain patterns

We use patterns measured at approximately ten times the mission operating frequency using a scale model of the Aquarius/SAC-D satellite (JPL, personal communication). Given the polarimetric nature of the radiometers, there are 12 gain patterns. They consist of 4 complex parameters (amplitude and phase) for each of the three beams, namely the copol and crosspol for the v - and h -pol. They are sampled at 0.5° resolution in spherical coordinates (θ, ϕ) (see also [9]). Figure 7. shows the total gain (i.e. sum of the copol and crosspol gains) of the inner beam. It also illustrates the domain in which the Sun will be moving during ones year of orbiting and shows that the Sun is located in relatively low gain areas, far from the boresight.

The scale model patterns are the latest and best estimates available of what will be those for the Aquarius antenna. They differ slightly from those obtained from simulations ignoring the platform that are reported in [9]. This is mentioned to emphasize that our results are necessarily sensitive to the accuracy of the patterns, and this issue will be discussed briefly in section III.B.

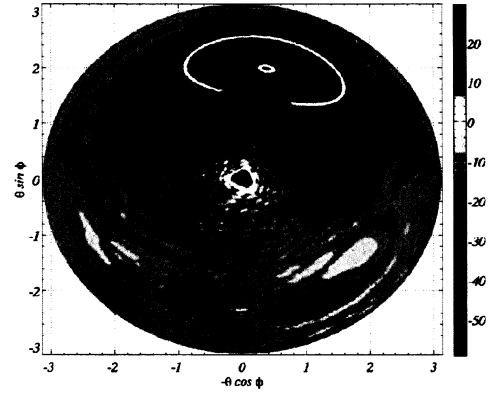


Figure 7. total gain of the inner antenna (in dB) with superimposed, the limits of the Earth FOV (black circle), and the limits of the domains inside which the Sun and the specular point travel during one year (yellow and red ellipsoids respectively). The antenna boresight is the dark red area at the center of the figure.

E. Surface spectrum

We use here the Durden and Vesecky [5] spectrum model, multiplied by a factor of two. The model was developed on a semi-empirical approach, using the theoretical form of Pierson and Moskowitz [10] for the large scales and a form compatible with the Philips [11] equilibrium spectrum and that allows deviation from it for the small scales. It was then adjusted, through parameters, to fit scatterometer data at 13.9 GHz, and to be compatible in order of magnitude with the slope variances estimated from visible measurement by Cox and Munk [12]. Yueh [6] suggested multiplying the spectrum by a factor of two to be in better agreement with SSMI measurement and a few studies suggested that the Cox and Munk slope variances may be underestimated due to the fact that their measurements did not account for all the roughness scales. This is the reason why Etcheto et al [13] include a version of this spectrum with the factor of two (in addition to the original one) when comparing radiometric measurements at L-band with T_b simulation. They find no definitive conclusion on the spectrum models validity, due to the dispersion in the data, but they illustrate that the original model leads to noticeable underestimation of the signal, while including the factor of two leads to a reasonable agreement between the model and the data. As we want to derive an upper bound for the glint contamination, we choose to multiply the spectrum by a factor of two. But it should be noted that it could result in some overestimation of the Sun T_a .

III. THE SUN IMAGE INFLUENCE ON AQUARIUS MEASUREMENTS

A. Position and extent of the Sun image

Figure 8. illustrates the variability of the position of Sun image and its location with respect to the antenna boresight. The Sun image position is defined here as the position of the specular point (which in the case of the rough surface corresponds to the location of the image of the center of the Sun). One sees a seasonal cycle corresponding to the change in position of the Sun itself, with a large variability at the solstices and a small one at the equinoxes. The Sun image gets relatively closer to the boresight in the middle of summer, but overall, the position of the Sun image is reasonably far from the main beam (more than 71° off the boresight). However, contrary to the Sun itself, which has a small angular extend, its image can spread over large areas on the Earth surface when one takes into account surface roughness. This spreading can potentially bring some parts of the Sun image significantly closer to the main beam than the center of the image.

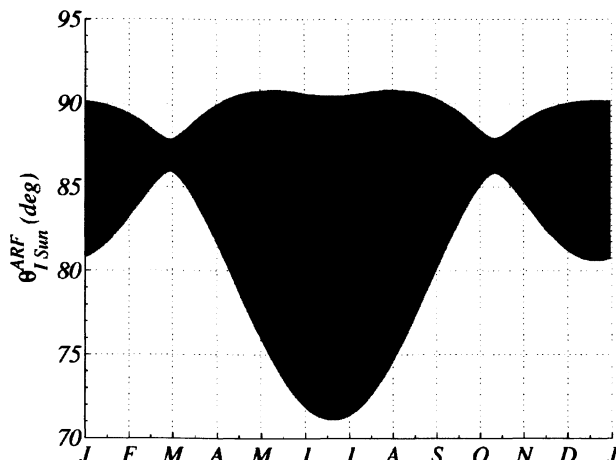


Figure 8. angle between the antenna boresight (inner beam) and the center of the Sun glint image (same graphic convention as Figure 2.).

Figure 9. shows the equivalent brightness temperature at the surface of the Earth surface due to the Sun glint for one of the extreme configurations, a Sun elevation of 30° . The *GO* model (top) results in a large Sun image that fills a significant portion of the FOV. However, despite the fact that the edge of the Sun image gets relatively close to the antenna boresight (indicated by the red arrow), the main beam is over an area where the brightness temperature of the scattered radiation is less than 0.01K. The areas of largest brightness temperatures (larger than 100 K) are located near the specular point and are in an area of very low antenna gain. The *TSM* results are significantly different. In this case, the largest T_b 's are still in the vicinity of the specular point, so still far from the main beam, where the antenna gain is low. But now, scatter from the surface under the boresight has a T_b close to 0.1 K, an order of magnitude larger.

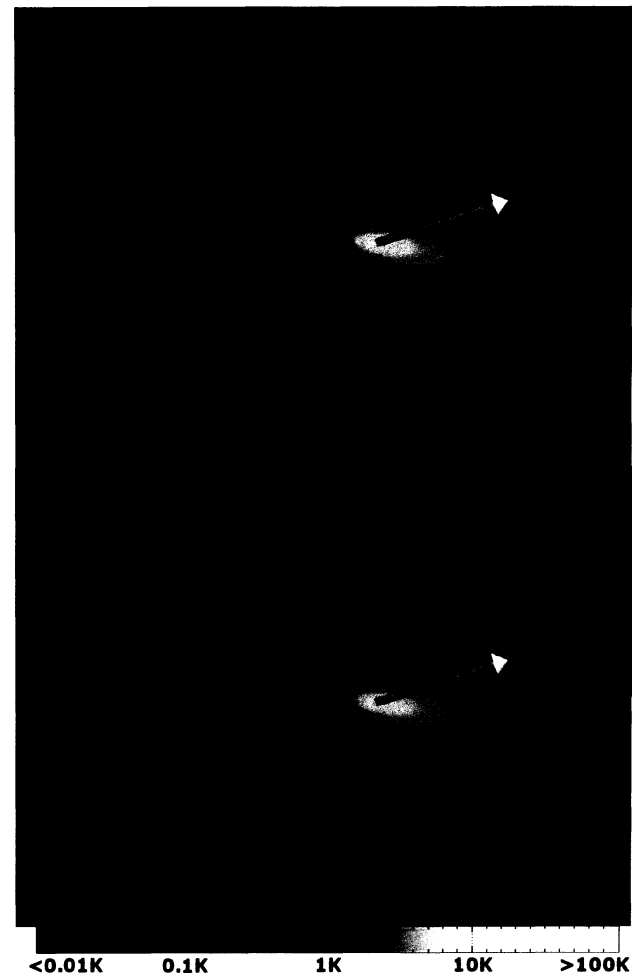


Figure 9. intensity of the glint at the Earth surface according to the *GO* model (top) and the *TSM* (bottom). The satellite is at the center of the reference frame, set up by the black arrow (satellite heading vector), the green arrow pointing to the right (satellite angular momentum) and upward green arrow (zenith direction). The red arrow is in the direction of the boresight of the inner beam. The yellow arrow starts at the specular point location and point towards the Sun (here at an elevation $\alpha \sim 30^\circ$). The colored disk on the Earth is the FOV, and the colorscale represents the surface equivalent brightness temperature induced by the scattering of the Sun radiation toward the instrument.

B. Dependence on Wind Speed and Sun Elevation

Figure 10. and Figure 11. report the antenna temperature due to reflected (scattered) radiation from the Sun as a function of the Sun elevation (α in Figure 1.). Results are shown for each of the models assuming a homogeneous wind speed of 8 m/s at 10 m height (azimuthal variation is neglected). The results were obtained using the Aquarius orbit and running the computations for one year in order to include all sun angles. The surface was assumed to be all ocean (effect of land which modifies some cases is discussed in section III.C). Three very different situations can be identified. When the Sun elevation is

low (domain III on the figures), all models predict a very small Sun contribution (less than 0.02 K for all beams, both polarizations). When the Sun is high above the horizon, the glint contamination generally becomes much larger, and some large differences between the various models arise.

The results obtained using the *GO* and *TSM* exhibit a trend in elevation whereas the specular point model appears randomly variable. The *GO* and *TSM* treat the Sun image as an extended source, and thus they average the bumps and valleys of the antenna gain occurring with high spatial frequency in the sidelobes. Consequently, the contribution from the Sun image follows the large trends in the antenna gain: it increases when part of the Sun image is getting close to the main beam, and remains small otherwise. In contrast, the specular point model treats the Sun as a point source. The specular point never gets close to the main beam, but it moves significantly over bumps and valleys of the antenna back lobes (Figure 7.). Therefore, the contribution derived from this later model is very variable and not noticeably dependent on the Sun elevation, but is more directly related to what particular bump or valley in the gain faces the specular point.

The *TSM* predicts the largest T_a of the three models at both polarizations. With this model, scattering of the Sun radiation occurs at any location on the illuminated FOV, towards all directions. So when the Sun elevation is large enough (around 3.5° for the inner beam, of the order of 6° for the outmost beam, see Figure 13.), the illuminated area drifts towards the antenna boresight and some Sun radiation is scattered backward into the main beam. Even if a very small fraction of radiation is scattered (of the order of -20 dB), T_b and the antenna gain prove to be large enough to induce a significant contamination in v -pol. It is larger than the Aquarius goal of 0.05K contamination by the sun, during 8% of the time. The results for the v -pol (Figure 10.) are different from those of the h -pol (Figure 11.). As illustrated in Figure 4., when the emerging angle is far from the specular reflection angle, the scattering coefficients at h -pol are much less than those in v -pol. Consequently, the results in h -pol are more similar between all models than in v -pol which is dominated by the small-scale contribution. Note however that the *TSM* has been found to underestimate backscattering measurements in h -pol [14][15].

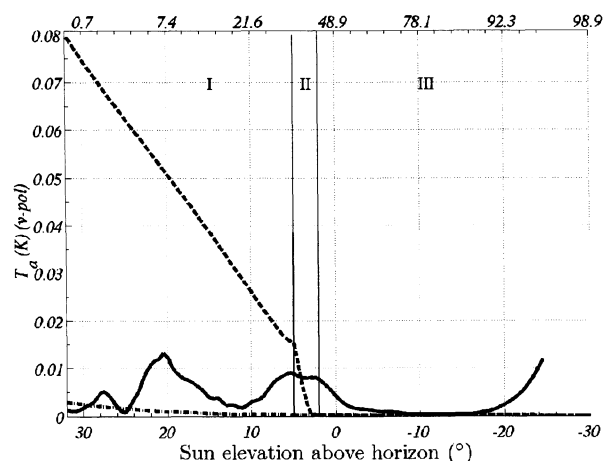


Figure 10. inner beam Sun glint antenna temperature in vertical polarization versus the Sun elevation angle α . The vertical dashed line illustrates the different regimes (see text) related to the position of the illuminated area with respect to the main beam. The upper x-axis reports the cumulative percentage of Sun occurrence at a given elevation angle (eg. the Sun is 21.9% of the time at elevation larger than 10°). The wind speed is 8 m/s at 10 m height.

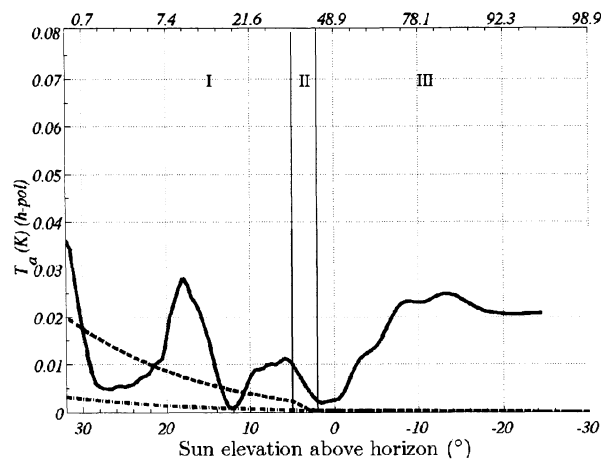


Figure 11. same as Figure 10. for the horizontal polarization.

The *GO* and specular models predict similar order of magnitude, although the *GO* model estimate is usually less than that of the specular model, especially at very low elevations, when part of the Sun image created by the roughness is outside of the antenna FOV. The *GO* model is relatively accurate for predicting the Sun contribution when the latter is dominated by the area near the specular point, namely for low Sun elevation. However, when the illuminated area reaches high-gain regions (when antennas point to the illuminated side), this model dramatically underestimates the glint because of the absence of small-scale scattering,

Figure 12. compares the contribution to T_a from the main beam only and the entire FOV in the case of large elevation angles (where the contamination is largest) using the *TSM*. For

this purpose, the main beam is defined to be the part of the antenna pattern where the gain is not less than 30 dB of its value at boresight. In the case of the Aquarius antennas that corresponds to an aperture of $\pm 10^\circ$, and accounts for more than 95 % of the total power. As illustrated in Figure 12., at high elevation angles, most of the contamination of T_a comes from to the main beam. The main beam corresponds to an area on the Earth surface with a diameter of the order of 600 km and an accurate correction for the contamination will require information about the surface conditions over this area centered in the direction of the boresight.

The dependence of the Sun glint T_a on the azimuth angle depends on the model. The specular point model is as critically sensitive to the azimuth angle as it is to elevation angle (for the same reasons). The *GO* model is also sensitive to the azimuth, and the curves reported Figure 10. and Figure 11. would vary by up to $\sim 0.01\text{K}$ when the Sun azimuth varies. However, this model always predicts a contamination largely less than 0.05 K, for any Sun azimuth angle. The *TSM*, which we consider to be the most realistic model, is insensitive to the Sun azimuth angle. First the extended image of the Sun tends to damp most of the azimuthal variations induced by the backlobes. Second, most of the signal actually comes from the main beam that is very azimuthally isotropic.

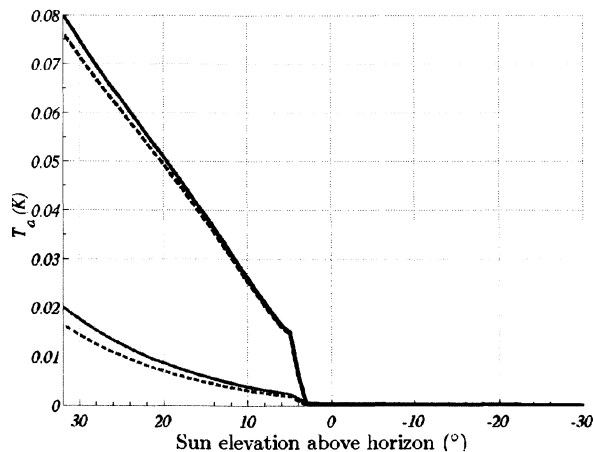


Figure 12. inner beam Sun glint antenna temperature in v-pol for a wind speed of 8 m/s at 10 m height. The T_a is computed accounting for the whole antenna FOV (plain line) or the main beam only (dashed line)

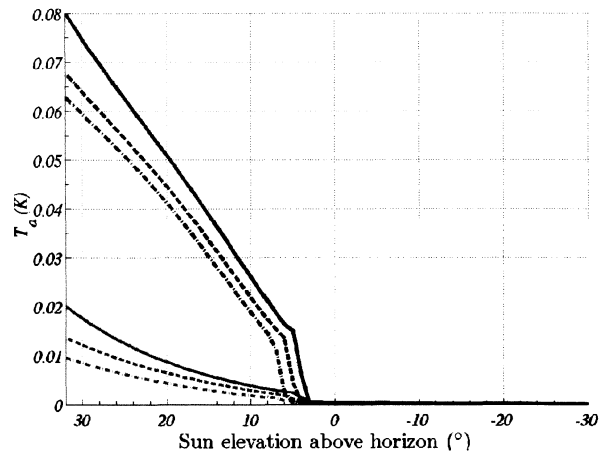


Figure 13. Sun glint antenna temperature for the inner (plain line), middle (dashed line) and outer (dashed-dotted line) beams. Wind speed is 8 m/s at 10 m height. Black curves are for v-pol, grey ones are for h-pol.

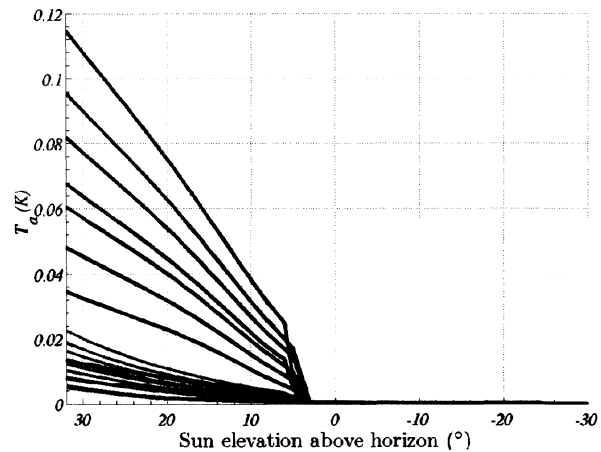


Figure 14. inner beam Sun glint T_a for the following wind speeds (at 10 m height), bottom to top: 0.7, 1, 3, 5, 7, 8, 10, 12 and 15 m/s. Black curves are for v-pol, grey ones are for h-pol.

Figure 14. illustrates the dependence of Sun contamination on wind speed. It shows that the three regime behavior is present at almost all wind speeds. Significant contamination (i.e. larger than 0.05 K) occurs at wind speeds as small as 5 m/s and contamination larger than 0.1 K occur for wind speeds that are not uncommon.

C. GlobalResults

The highest contamination occurs at high latitudes of the northern hemisphere during seasons when the sun angle is high. In such locations, it is very likely that significant portion of the antenna FOV will be over land/ice with much different scattering properties than ocean. In this section we account for the presence of land surface in the antenna FOV when computing the Sun glint T_a .

In order to bound the problem, we assume that no reflection occurs on land surfaces and set the surface brightness temperature to zero for every pixel where land surface is present. For the reflectivity at the ocean pixels, we use the *TSM* and assume a homogeneous wind speed of 8 m/s. To locate the land surfaces, we use a land/sea mask at 15 arcmin resolution (derived from the GTOPO 30 data). We focus here in the area and time where the contamination is considered significant enough to potentially hinder SSS retrieval. We set the threshold for this to be $T_{a\max} = 0.05\text{K}$, a value that translates roughly into 1 psu uncertainty. Figure 10. shows that $T_{a\max}$ is reached or exceeded in v-pol at $U10 = 8\text{ m/s}$ when the Sun elevation is larger than $\sim 20^\circ$ and this happens only between April, 21 and August, 21 (Figure 2.) and only when the satellite is at the high latitudes of the northern hemisphere (not shown).

Figure 15. shows a 25 minute portion of an orbit over the northern hemisphere during one such period. The Sun glint T_a for the three Aquarius beams are reported in Figure 16. as a function of distance along the track. The Sun glint T_a is small when the FOV is dominated by land and varies a little bit over the ocean as the latitude changes. The transitions between land and ocean signal are very abrupt as they occur over very short distances. This is due to the fact that most of the signal comes from a limited area around the boresight (Figure 12.). That means that the modulation of the Sun glint T_a by land will be small, and that the signal will be mostly driven by the Sun elevation and its brightness temperature. Notice two relatively large changes in the signal that occur at the locations identified by the diamond and circle in both Figure 15. and Figure 16. In these cases, the boresight does not encounter a transition land/ocean. The change in T_a is due to the presence of a land/sea transition in the vicinity of the boresight, and is limited to a change of the order of 0.02 K.

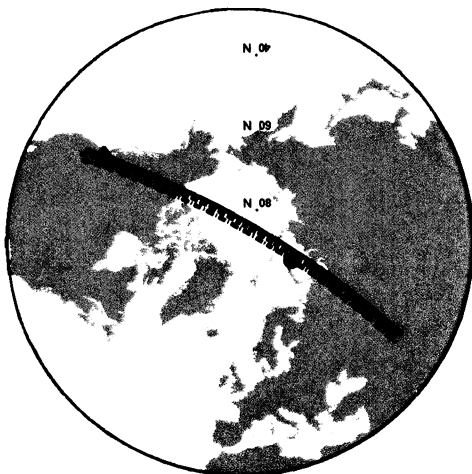


Figure 15. tracks on the Earth surface of the inner (plain line), middle (dashed line) and outer (dashed-dotted line) beams on the 06/04/2009 between 01:46:50 and 02:12:20. The filled diamond and circle report the same two locations of interest as in Figure 16. that are discussed in the text.

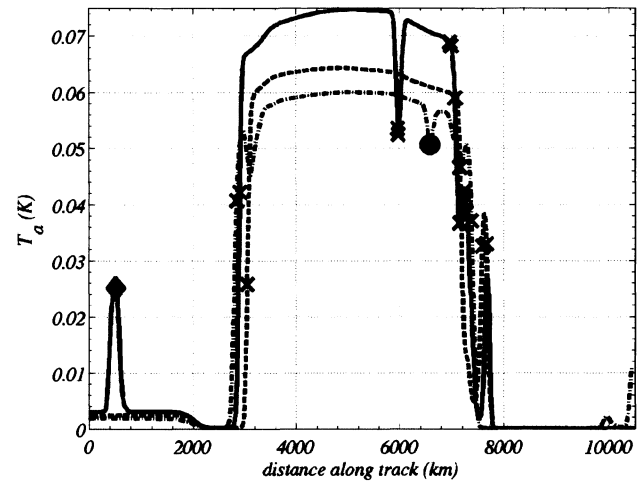
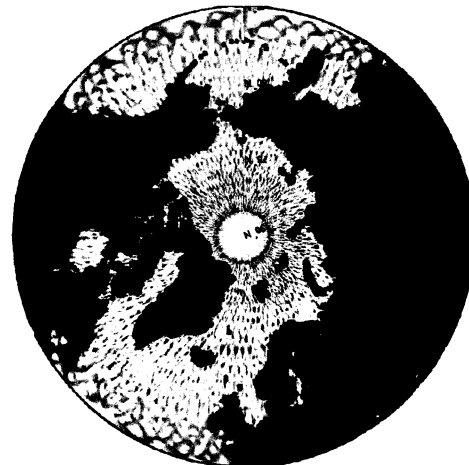


Figure 16. Sun glint contamination for the inner (plain line), middle (dashed line) and outer (dashed-dotted line) in v-pol versus the distance along track. The tracks on Earth for the three beams are reported in Figure 15. The crosses \times report the location where a transition between land and sea occurs. The filled diamond and circle report the same locations as on Figure 15. and are discussed in the text.

The Figure 17. reports the Sun glint T_a averaged over one month for the mid- and high-latitudes of the northern hemisphere. The data includes all the three beams. The figures shows that no particularly large influence of land can be noticed at large distance from the coast. Some linear features in the map are due to the different sensitivity of the different beams to the Sun glint. Such stripping could also be present in the retrieved SSS. Finally, as expected from the Sun elevations reported in Figure 2. , the month of June exhibits generally larger contamination than the month of May. Note that the month of July and August (not shown) exhibit patterns very similar as June and May respectively.



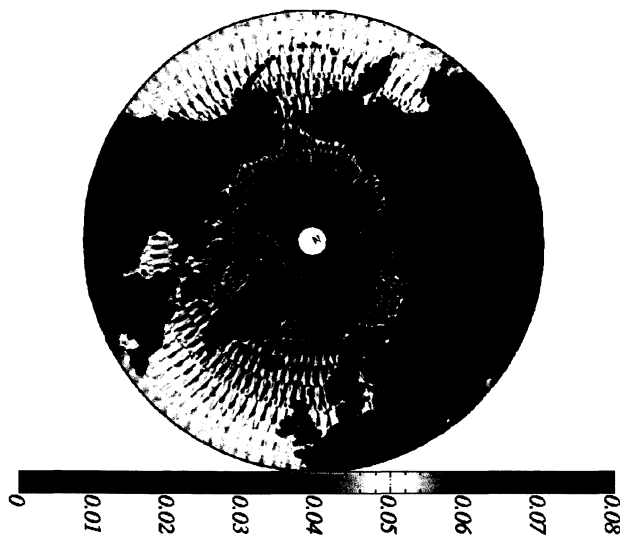


Figure 17. monthly average maps of the Sun glint in v-pol for (top) May and (bottom) June.

IV. CONCLUSIONS AND PERSPECTIVE

We show that the scattering of Sun radiation from the Earth surface has to be considered in order to account properly for the Sun contamination of the Aquarius measurements. The Sun contamination after reflection on the Earth surface is small, but not always negligible if one considers the demanding accuracy needed for salinity retrieval (e.g. 0.1 K). We find also that it is important to account for the small scale roughness which can significantly increase the potential for contamination. Contamination can noticeably exceed the budgeted value of 0.05 K when the bistatic scattering allowed by the rough nature of the ocean surface is included in the analysis. We show that most of the contamination is due to the scattering that reach antennas through the main beam when the footprint of the antennas is illuminated by the sun. Despite the fact that we have used hypotheses for a worst case scenario, and that large contamination may be rare, it will be necessary to correct for this effect at some times, at least partially. Since the surface roughness and the antenna gain will have to be very well known in the main beam direction independently of the Sun contamination issue, the constraint for an accurate Sun glint correction will be on the accuracy on the Sun brightness temperature. In the near future, the model presented here is to be included in the complete mission simulator that includes complex and realistic scenes for the Earth surface. We will also take into account the Sun brightness temperature variability. Future advanced simulations, including retrieval exercises, will allow us to develop mitigation or correction strategies. Similar techniques will be employed for addressing other potential source of contamination, like the Moon or the galaxy.

V. A. AKNOWLEDGEMENT

We would like to thank Joe Vacchione (for providing the antenna patterns) and Paolo de Matthaeis for support in gridding the antenna pattern data.

REFERENCES

- [1] D.M. Le Vine, G.S.E. Lagerloef, R. Colomb, S. Yueh, F. Pellerano, "Aquarius: An Instrument to Monitor Sea Surface Salinity from Space", *IEEE Trans Geosci. & Remote Sens.*, submitted and revised, 2007.
- [2] Yueh, S.H.; West, R.; Wilson, W.J.; Li, F.K.; Njoku, E.G. & Samii, Y.R. Error sources and feasibility for microwave remote sensing of ocean surface salinity *IEEE Transactions on Geoscience and Remote Sensing*, 39, 1049-1060, 2001.
- [3] Le Vine, D.M., Abraham, S., Wentz, F. and Lagerloef, G.S.E., "Impact of the Sun on remote sensing of sea surface salinity from space", *IGARSS '05. Proceedings*, July 2005.
- [4] Reul, N., Tenerelli, J., Chapron, B., and Waldteufel, P., "Modeling Sun Glitter at L-Band for Sea Surface Salinity Remote Sensing With SMOS" *Geoscience and Remote Sensing*, *IEEE Transactions on*, Vol. 45(7), 2073 - 2087, 2007.
- [5] Durden, S. L., et J. F. Vesecky, "A physical radar cross-section model for a wind-driven sea with swell", *IEEE Journal of Oceanic Engineering*, OE-10, 445-451, 1985.
- [6] Yueh, S. H., "Modeling of wind direction signals in polarimetric sea surface brightness temperatures", *IEEE Trans on Geosci. & Remote Sens.*, 35, 1400-1418, 1997.
- [7] Guidice, D. A., Cliver, E. W., Barron, W. R., Kahler, S., "The Air Force RSTN System", *Bulletin of the American Astronomical Society*, Vol. 13, p.553, 1981.
- [8] <http://www.ngdc.noaa.gov/stp/SOLAR/ftp/solarradio.html>
- [9] Dinnat, E.P. and D.M. Le Vine, "Effects of the Antenna Aperture on Remote Sensing of Sea Surface Salinity at L-band", *IEEE Transactions on Geoscience and Remote Sensing*, 45, 2051 - 2060, 2007.
- [10] Pierson, W. J., Jr., and Moskowitz, L., "A proposed spectral form for fully developed wind seas based on the similarity theory of S. A. Kitaigorodskii", *Journal of Geophysical Research*, 69, 5181-5190, 1964.
- [11] Phillips, O. M., The equilibrium range in the spectrum of wind-generated waves, *Journal of Fluid Mechanics*, 4, 426-434, 1958.
- [12] Cox, C., and Munk, W., "Measurement of the roughness of the sea surface from photographs of the sun's glitter", *Journal of the Optical Society of America*, 44, 838-850, 1954.
- [13] Etcheto, J., Dinnat, E., Boutin, J., Camps, A., Miller, J., Contardo, S., Wesson, J., Font, J., and David Long, "Wind speed effect on L-band brightness temperature inferred from EuroSTARRS and WISE 2001 field experiments", *IEEE Transactions on Geoscience and Remote Sensing*, 42(10):2206-2213, October 2004.
- [14] Janssen, P. A. E. M., H. Wallbrink, C. J. Calkoen, D. Van Halsema, W. A. Oost, and P. Snoeij, "VIERS-1 Scatterometer model", *J. Geophys. Res.*, 103, 7807-7831, 1998.
- [15] Plant, W. J., "Bragg scattering of electromagnetic waves from the air/sea interface", in *Surface Waves and Fluxes, Remote Sensing*, Vol. 2, edited by Geernaert, G. L. and Plant, W. J., Kluwer Academic, , 41-108, 1990.